Applied Surface Science Advances 12 (2022) 100337

Contents lists available at ScienceDirect

Applied Surface Science Advances

journal homepage: www.sciencedirect.com/journal/applied-surface-science-advances

Fabrication of dual Z-scheme g-C_3N_4/Fe_2TiO_5/Fe_2O_3 ternary nanocomposite using natural ilmenite for efficient photocatalysis and photosterilization under visible light

Charitha Thambiliyagodage [a,*], Anura Kumara [b], Madara Jayanetti [a], Leshan Usgodaarachchi [c], Heshan Liyanaarachchi [a], Buddi Lansakara [d]

[a] Faculty of Humanities and Sciences, Sri Lanka Institute of Information Technology, Malabe, Sri Lanka
[b] Department of Physical Sciences & Technology, Faculty of Applied Sciences, Sabaragamuwa University of Sri Lanka, Belihuloya, Sri Lanka
[c] Department of Materials Engineering, Faculty of Engineering, Sri Lanka Institute of Information Technology, Malabe, Sri Lanka
[d] Department of Nano Science Technology, Wayamba University of Sri Lanka, Kuliyapitiya, Sri Lanka

ARTICLE INFO

Keywords:
Ilmenite
g-C_3N_4
Z-scheme
Photodegradation
Photosterilization

ABSTRACT

The advanced oxidation process is a prominent method available to remove dyes released to normal water reservoirs to alleviate water scarcity. We report the fabrication of novel g-C_3N_4/Fe_2TiO_5/Fe_2O_3 using natural ilmenite sand as the precursor of the metallic semi-conductors exploration of a heterostructure for photo-degradation of methylene blue under sunlight. Ternary composites were synthesized by varying g-C_3N_4 with respect to Fe_2TiO_5/Fe_2O_3 and varying Fe_2TiO_5/Fe_2O_3 with respect to g-C_3N_4 where the varying component was varied as 8, 24 and 40%, respect to the constant material. The hybridization of the three semi-conductors has been confirmed by the microscopic, chemical, and structural analyses. X-ray diffraction patterns show the presence of all three g-C_3N_4, Fe_2TiO_5 and α-Fe_2O_3 while the transmission electronic microscopic and scanning electronic microscopic images show the heterogeneous distribution of the metal oxide nanoparticles on g-C_3N_4 matrix forming the composite. HRTEM images further reveal the junction of Fe_2TiO_5 and α-Fe_2O_3. X-ray photoelectron spectra show the existence of s-triazine and heptazine rings in the composites with Fe^{3+} and Ti^{4+} as the only oxidation states of Fe and Ti. Fe_2TiO_5/Fe_2O_3/40% g-C_3N_4 with bandgap of 2.63 eV calculated by diffuse reflectance UV-Visible spectroscopy showed the highest photocatalytic activity (0.009 min^{-1}) being 1.3 times greater than the Fe_2TiO_5/Fe_2O_3 nanoparticles. Enhanced photocatalytic activity over the fabricated composites was observed due to the increased visible light absorption, efficient charge separation and improved charge transportation. g-C_3N_4 coupled with 40% Fe_2TiO_5/Fe_2O_3 showed the highest antibacterial activity against gram-negative *E.Coli*. The synthesis of dual Z-scheme g-C_3N_4/Fe_2TiO_5/Fe_2O_3 ternary composite provides new sights in developing novel photocatalysts using natural ilmenite sand for environmental applications.

1. Introduction

Water scarcity is a massive issue faced by the world which deteriorates the quality of living of all living beings. Rapid industrialization caused by anthropogenic activities causes the discharge of various hazardous compounds including but not limited to heavy metals, pesticides, fertilizers, pharmaceuticals, and dyes. Among them, dyes released by paper, paint, textile, cosmetics, and plastic industries to the normal water reservoirs play a crucial role [1,2]. Dyes cause severe harmful effects due to their accumulation in the water bodies as they are non-biodegradable because of their complex and synthetic nature [3,4]. Briefly, such hazardous effects include but are not limited to alterations in the biological and chemical oxygen demand [5], reduction of the light penetration into the water bodies limiting the photosynthesis [6,7], and collection of toxic materials such as heavy metals, chlorinated compounds, surfactants, salts, etc. [8]. Further, the presence of dyes affects the aesthetic value [9]. Therefore, it is important to remove dyes from wastewater and several methods including adsorption [10,11], oxidation [12,13], coagulation [14,15], nanofiltration [16,17]. However, these methods collectively exhibit different drawbacks like

* Corresponding author.
E-mail address: charitha.t@sliit.lk (C. Thambiliyagodage).

https://doi.org/10.1016/j.apsadv.2022.100337
Received 15 June 2022; Received in revised form 3 November 2022; Accepted 8 November 2022
Available online 11 November 2022

non-destruction of pollutants, non-selective, high cost, resistance to treatment, formation of intermediates, sludge generation, membrane fouling, and insufficient separation [18,19]. The advanced oxidation process is advantageous over other methods as the dyes are degraded into harmless products by the different radicals generated; hydroxyl radicals ($OH^{\bullet}$) and superoxide radicals ($O_2^{-\bullet}$) which are being widely used for photoreduction [20–22]. The heterogeneous photocatalysis garnered extensive attention as sunlight can be used as the energy source for the production of above mentioned radicals which will further degrade the pollutant molecules [23]. g-C_3N_4 has been tremendously employed in the field of photocatalysis recently due to its visible activity that was first reported by Wang et al. [24] in which it was used as the photocatalyst to produce H_2 and O_2 by splitting water under sunlight. g-C_3N_4 consists of s-triazine or tri-s-triazine as the monomers which are interconnected via ternary amines to build 2D sheets. Atoms of one sheet are linked via covalent bonds and the sheets are held together via Van der Waals forces. The valence band (VB) of g-C_3N_4 is comprised of N 2p level, while the conduction band (CB) is made by the hybridization of the N2p and C 2p levels. Therefore, the photogenerated electrons at the CB recombine with the holes in the VB easily leading to poor photocatalytic activity. However, to overcome such drawbacks g-C_3N_4 is coupled with semiconductor metal oxides to enhance the charge carrier separation which would then produce a higher photocatalytic activity. In order to succeed such interest g-C_3N_4 has been coupled with TiO_2 [25,26], ZnO [27,28], iron oxide [29,30], tin oxide [31,32], WO_3 [33,34], V_2O_5 [35,36], $CoFe_2O_4$ [37], Ag/ZnO nanowires/Zn [38] etc. Dual Z-scheme structures in which g-C_3N_4 is included are also reported to be efficient photocatalysts such as g-C_3N_4/$Bi_4Ti_3O_{12}$/$Bi_4O_5I_2$ [39], g-C_3N_4/Ag_3PO_4/Ag_2MoO_4 [40], WO_3/g-C_3N_4/Bi_2O_3 [41], g-C_3N_4/Ag_2CO_3/graphene oxide [42] for H_2 production, O_2 evolution, tetracycline degradation, methylene blue degradation etc. The main concern with the selected most of semiconductors is that they are sensitive to UV light only and that limits the efficiency of the overall photocatalysts though g-C_3N_4 is visible active, and the possible electron hole pair recombination. Therefore, we got interested in fabricating a novel photocatalyst where the semiconductor metal oxides are also active in the visible range. Natural ilmenite abundantly available on sea beaches of Sri Lanka is primarily being used only for exporting to synthesize pure TiO_2 used as the white pigment. During the production of commercial TiO_2, acid leachate is discarded as a waste material which highly corrosive but contains a high concentration of iron and titanium. In our previous studies, we demonstrated the synthesis of novel photocatalysts using acid leachate giving more value to ilmenite sand [43,44]. Fe_2O_3 alone and coupled to other semiconductors and carbon based nanomaterials have also been reported to photocatalytically active in the visible range and degrade the pollutants in water [45,46].

Here, we report the coupling of Fe_2TiO_5/Fe_2O_3 heterostructures with g-C_3N_4 for an enhanced photocatalytic activity for the photodegradation of methylene blue and the antibacterial activity of the synthesized nanocomposites against *E.Coli*. Moreover, g-C_3N_4 is reported to be coupled with only one semiconductor metal oxide creating either type II or z-scheme heterojunctions and coupling g-C_3N_4 with two metal oxides is not well reported in the literature. According to our knowledge, this is the first time that the synthesis, characterization and photocatalysis of g-C_3N_4/Fe_2TiO_5/Fe_2O_3 is presented.

2. Procedure

2.1. Synthesis of Fe_2TiO_5/Fe_2O_3

Ilmenite sand 10 g was treated with 200 ml of conc. HCl under refluxing conditions at 90°C with continuous magnetic stirring for 6 hours followed by stirring at room temperature for another 18 hours. Obtained leachate was separated and the residue was again treated with a new portion of 200 ml of HCl. This procedure was repeated two times except for 100 ml of HCl was used instead of 200 ml. Obtained all four leachates were combined and conc. NH_3 was added dropwise until pH reaches 10. Obtained brown colour precipitate was washed with distilled water until the washings were negative for Cl^- and a neutral pH is reached. The resulting precipitate was annealed at 800°C for 2 hours. This product will be abbreviated as FF in the text.

2.2. Synthesis of g-C_3N_4

Urea was annealed at 550°C for 2 hours in an N_2 atmosphere and the obtained yellow colour product was washed with distilled water and ethanol. The dried product is denoted as GC in the text.

2.3. Synthesis of Fe_2TiO_5/Fe_2O_3/g-C_3N_4

Synthesized Fe_2TiO_5/Fe_2O_3 and g-C_3N_4 were mixed in different weight percentages where Fe_2TiO_5/Fe_2O_3 was added as 8%, 24%, and 40% with respective to g-C_3N_4 which are abbreviated as FF8GC, FF24GC and FF40GC, and g-C_3N_4 was mixed with Fe_2TiO_5/Fe_2O_3 in weight percentages of 8%, 24%, and 40% with respective to Fe_2TiO_5/Fe_2O_3 and they are denoted as FFGC8, FFGC24 and FFGC40. Mixed samples were sonicated at 24 kHz frequency (50 W) for 20 minutes and were treated hydrothermally at 150°C for 12 hours. The obtained sample was washed with ultrapure water and dried at 60°C.

2.4. Photocatalytic activity

Synthesized photocatalysts (100 mg) were shaken in 100 ml of 10 ppm MB solution for 90 minutes in dark to reach the adsorption-desorption equilibrium. Then the catalysts containing MB solutions were exposed to sunlight between 10.00 a.m. to 2.00 p.m. Intensity of sunlight was in the range of 80000 - 1200000 lux during the experiments. Experiments was carried out for 150 minutes and aliquots were withdrawn every 15 minutes and absorbances were measured by a UV-Visible spectrophotometer.

2.5. Antibacterial activity

Microbial strain and inoculum preparation

The test microorganism *E.Coli* was procured from Medical Research Institute, Sri Lanka. *E.Coli* was cultured in nutrient broth at 37°C overnight. The bacterial cultures were sub-cultured before the assay and later diluted to obtain a bacterial suspension of 5×10^{-5} colony-forming units (CFUs)/mL for further analysis.

Broth dilution assay

The antibacterial activity of GC, FF, FFGC40 and FF40GC composites was investigated using the Broth Dilution method against native and nanoparticle-treated bacteria to determine what inhibits the growth of *E. Coli*. The antibacterial effect of the composites was tested against *E. Coli* in a sterilized Nutrient Broth medium. For the Broth Dilution Assay, 24 h aged bacterial culture was adjusted to obtain 5×10^{-5} CFU/mL with a 0.5 McFarland turbidity standard as the visual yardstick and spectrophotometer. The adjusted bacterial suspension was used within 30 minutes to avoid changes in the cell count. Nanoparticle suspensions were prepared by sonicating the synthesized nanomaterials in deionized water for 1 h. 1 mL of the freshly prepared overnight culture was inoculated to 5 mL of sterilized Nutrient Broth medium containing 1 mL of 60 mg/mL of nanomaterial suspensions. Additionally, 1 mL of bacterial culture was inoculated to 5 mL of sterilized nutrient broth medium containing 1 mL of Amoxicillin (10 mg/mL) as the positive control. Nanocomposite-free broth medium inoculated with *E. Coli* served as the growth control. The Nutrient Broth medium with nanomaterials alone was retained as the blank. All tubes were incubated in a temperature-controlled shaker (150 rpm) at 30°C overnight for 24 h. After the incubation, O.D. (Optical Density) was recorded at 600 nm to measure the turbidity and the inhibition of growth was determined. The OD for each sample was calculated.

Percentage inhibition of growth was calculated using the formula given below:

$$\%\text{Inhibition} = \frac{(\text{O.D.})_{\text{control}} - (\text{O.D.})_{\text{test}}}{(\text{O.D.})_{\text{control}}}$$

Where,

(O.D.) control = absorbance of the control sample

(O.D.) test = absorbance of the test sample with the respective composite

3. Characterization

TEM images were collected using Tecnai G2 F20 Twin TMP using 200 KV accelerating voltage. Samples were prepared by dropping a diluted suspension of the nanomaterials onto the Cu grid. SEM images were obtained by Carl zeiss evo 18 research spectrophotometer equipped with Edax element eds system. XRD patterns were collected via the D8 Advance Bruker system using CuKα (λ = 0.154 nm) radiation varying 2θ from 5 °- 80 ° at a scan speed of 2 °/min and the Panalytical software was used for analysis. The samples' chemical composition was analyzed by X-ray fluorescence (XRF) using a HORIBA Scientific XGT-5200 X-ray analytical microscope, equipped with a Rh anode X-ray tube operated at a maximum voltage of 50 kV. The survey spectra and the higher resolution spectra of the synthesized catalysts were acquired by Thermo Scientific™ ESCALAB Xi$^+$ X-ray Photoelectron Spectrometer. Instrument was calibrated with pure graphite and charge was neutralized prior analysis. Peak fit 4 software was used to fit the peaks. The absorbance of MB samples was measured by a Shimadzu UV-1990 double beam UV-Visible spectrophotometer.

4. Results and dscussion

4.1. XRD analysis

XRD patterns were collected to study the crystallographic orientation of the synthesized materials (Fig. 1). The XRD pattern of pure g-C_3N_4 consists of two peaks at 13.1° and 27.4°, which are attributed to the (100) crystal plane of tri *s*-triazine units and to the (002) crystal plane which corresponds to the interlayer stacking of aromatic segments. Interlayer spacings calculated for the corresponding peaks are 0.67 nm and 0.33 nm, respectively. The crystallite size of the peak corresponds to the (002) plane is 3.86 nm. The peaks at 18.20°, 25.60°, 32.61°, 36.68°, 37.44°, 40.97°, 46.08°, 48.83°, 55.27°, 60.14° of the XRD pattern of FF

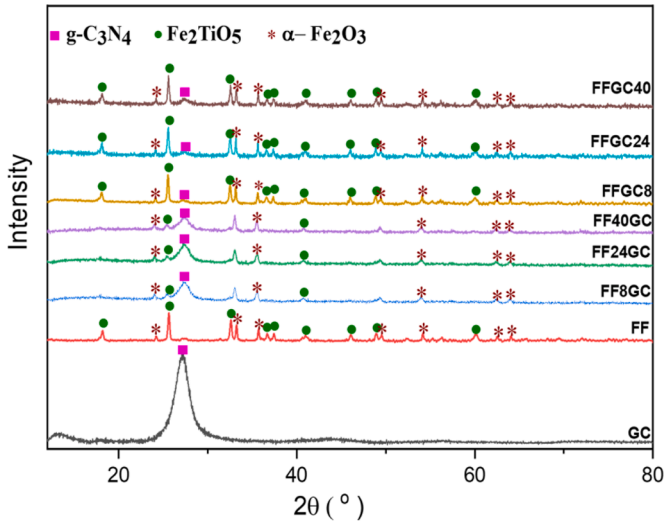

Fig. 1. XRD patterns of the synthesized nanomaterials.

are assigned to the (200), (101), (230), (301), (131), (240), (331), (430), (060), (232) planes of the orthorhombic phase of pseudobrookite, Fe_2TiO_5 (JCPDS card No: 41-1432). Calculated lattice parameters, a (9.800 Å), b (9.849 Å), c (3.720 Å) and the unit cell volume (359.0 Å^3) further indicated the formation of the orthorhombic Fe_2TiO_5. Peaks at 24.21°, 33.24°, 35.71°, 49.54°, 54.16°, 56.31°, 62.52° and 64.07° correspond to the (012), (104), (110), (024), (116), (018), (214), and (300) planes of α-Fe_2O_3 (JCPDS card No: 79-0007). Calculated lattice parameters, a (5.016 Å) and c (13.626 Å) and the unit cell volume (296.90 Å^3) are consistent with the values reported for the hexagonal α-Fe_2O_3 in the literature [47]. The peak at 27.37° is attributed to the (110) plane of the Rutile phase of TiO_2. The interlayer distance and the crystallite size of Fe_2TiO_5, 0.37 nm and 36.37 nm, respectively, were calculated using the peak at 25.60°. The same parameters of α-Fe_2O_3 and Rutile were calculated using the peaks at 33.24° and 27. 37°, respectively. The interlayer distance of α-Fe_2O_3 and Rutile was 0.27 nm and 0.33 nm, respectively. XRD patterns of FFGC8, FFGC24 and FFGC40, show the peaks corresponding to both Fe_2TiO_5 and α-Fe_2O_3 and the prominent peak of Rutile which appears at 27.37° is masked by the (002) plane of g-C_3N_4. The intensity of the peak assigned to the (002) plane increases going from FFGC8 to FFGC40 as the g-C_3N_4 proportion increases. The XRD patterns of FF8GC, FF24GC and FF40GC are dominated by the peak corresponding to the (002) plane of g-C_3N_4 as the weight of FF is varied while that of g-C_3N_4 kept constant and hence the dominant constituent of those composites is g-C_3N_4. Peaks corresponding to Fe_2TiO_5 and α-Fe_2O_3 were identified though the intensity was low as the percentage of FF ranges from 8-40 and is comparatively low.

4.2. TEM analysis

TEM images of GC and FFGC40 are shown in Fig. 2. TEM images of GC are shown in Fig. 2(a) and (b). Thin and fluffy g-C_3N_4 nanosheets are arranged as tremella-like layers as exhibited in Fig. 2(a). Mesopores are formed in the nanosheets as revealed in Fig. 2(b) due to the polymerization and the elimination of gas molecules during the annealing process. Insert of Fig. 2(b) clearly show the formed mesoporous structure. The nitrogen and oxygen in the reaction system can generate gas bubbles splitting the polymer when it polymerizes resulting in stripping g-C_3N_4 layers into small layers producing a fluffy structure [48,49]. Fig. 2(c) shows the aggregated metal oxide nanoparticles are heterogeneously distributed on the 2D nanosheets of g-C_3N_4. HRTEM shown in Fig. 2(d) shows the conjunction of Fe_2TiO_5 and α-Fe_2O_3. The interlayer distances of 0.35 and 0.48 nm indicate the (101) and (200) planes of Fe_2TiO_5 while the d spacing value of 0.27 nm indicates the (104) plane of α-Fe_2O_3.

4.3. SEM analysis

SEM images of the synthesized nanomaterials are shown in Fig. 3. SEM image of Fe_2TiO_5/Fe_2O_3 nanoparticles is shown in Fig. 3(a). Nanoparticles are worm-like shaped and interconnected due to Oswald ripening. Fig. 3(b) shows the SEM image of GC exhibits an interconnected macroporous structure. As shown in the TEM image given in Fig. 2(b) a well-developed mesoporous structure is established in g-C_3N_4. Therefore, synthesized it is evident that the synthesized g-C_3N_4 consists of a hierarchical porous structure. As shown in the SEM image of FFGC40 (Fig. 3(c)) the interconnected porous structure has been disturbed and the Fe_2TiO_5/Fe_2O_3 nanoparticles are agglomerated on the g-C_3N_4 nanosheets. The worm-like shape of the nanoparticles disappeared when subjected to hydrothermal conditions for 12 hours. EDX spectrum of Fe_2TiO_5/Fe_2O_3 (Fig. 3(d)) reveals the presence of Fe and Ti as the main metallic species and Mn is present in minor quantities being consistent with the XRF analysis reported below. EDX spectrum of FFGC40 (Fig. 3(e)) exhibits the presence of C and N in the g-C_3N_4 framework with Fe, Ti and Mn as the metallic species.

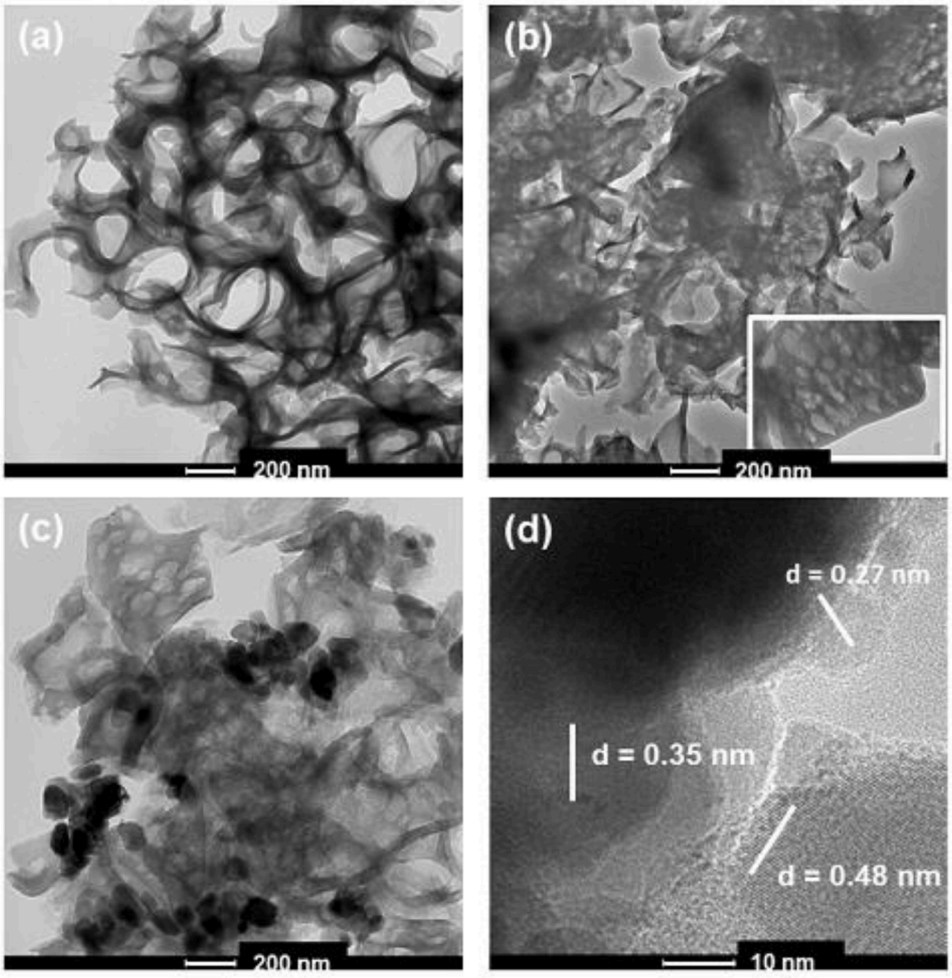

Fig. 2. TEM images of (a), (b) GC (c) FFGC40 (d) HRTEM images of FFGC40.

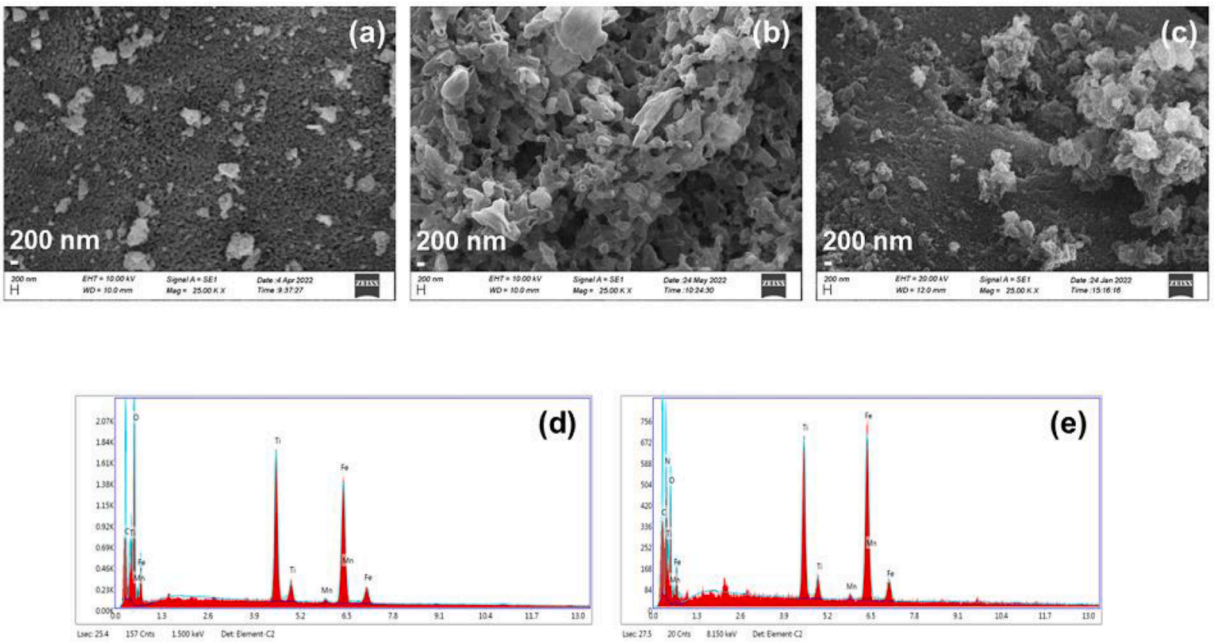

Fig. 3. SEM images of (a) Fe_2TiO_5/Fe_2O_3 nanoparticles (b) GC (c) FFGC40, EDX spectra of (d) Fe_2TiO_5/Fe_2O_3 nanoparticles (e) FFGC40.

4.4. XPS analysis

The surface of the prepared catalysts was analyzed by XPS (Fig. 4). The survey spectrum of GC (Fig. 4(a)) shows the presence of C, N and O as the main species while in addition to them Ti and Fe are present in the survey spectrum of FFGC40 (Fig. 4(b)). The higher resolution spectrum of C 1s of GC is given in Fig. 4(c) and is deconvoluted to three main peaks centered at 284.6, 288 and 293.4 eV, which are attributed to the sp^2 hybridized graphitic C (C-C), sp^2 hybridized carbon in N-C=N and π-π transitions, respectively. Similar chemical behaviour was observed in the higher resolution spectrum of C 1s of FFGC40 (Fig. 4(d)) in which the respective peaks appeared at 284.6, 288.2 and 293.7 eV, respectively. The higher resolution spectrum of N 1s (Fig. 4(e)) is deconvoluted to four peaks at 398.5, 400, 401 and 404 eV, which are assigned to sp^2

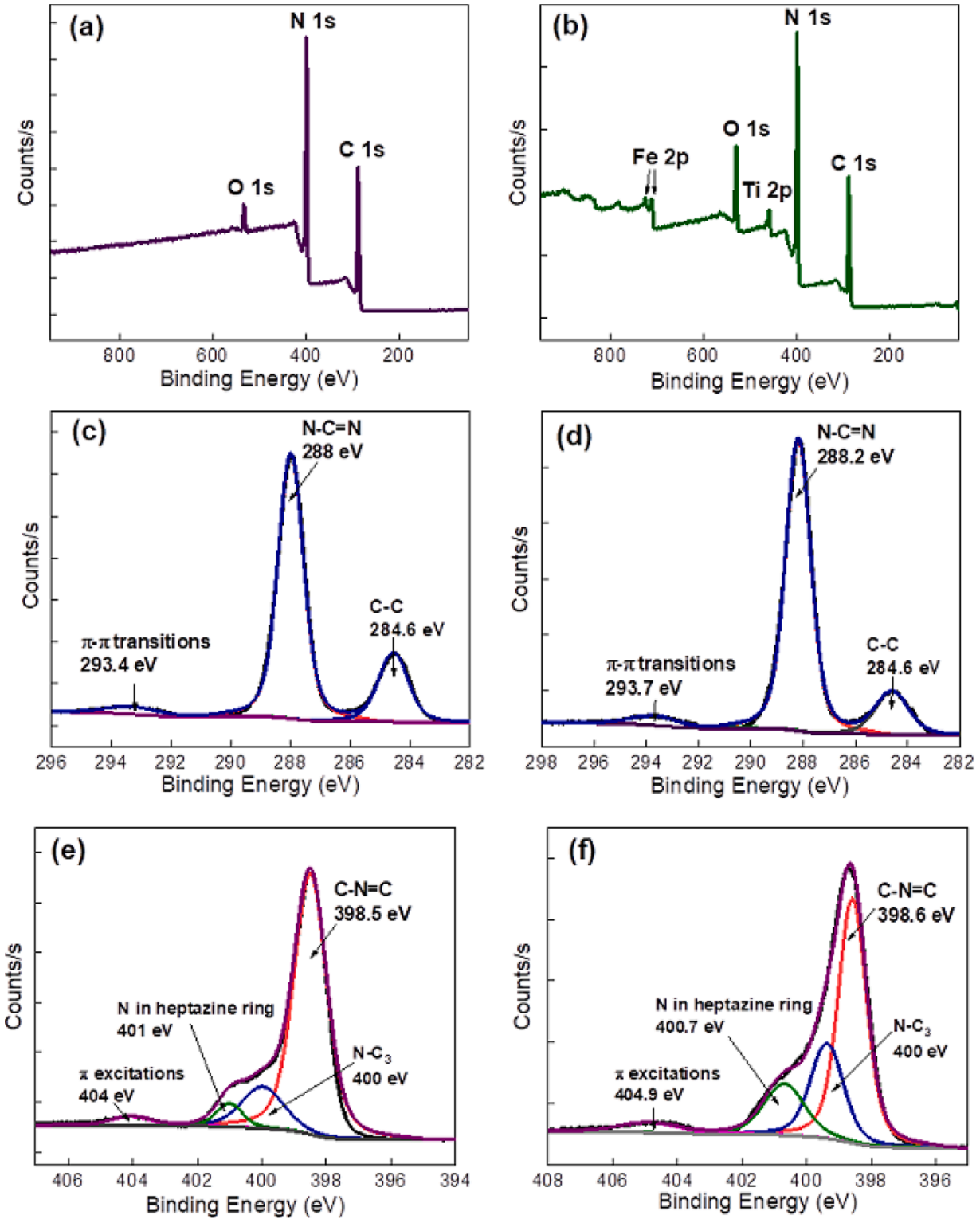

Fig. 4. Survey spectra of (a) GC (b) FFGC40, higher resolution spectra of C 1s of (c) GC (d) FFGC40, higher resolution spectra of N 1s of (e) GC (f) FFGC40, (g) higher resolution spectrum of Ti 2p of FFGC40, (h) higher resolution spectrum of Fe 2p of FFGC40 and higher resolution spectrum of O 1s of FFGC40.

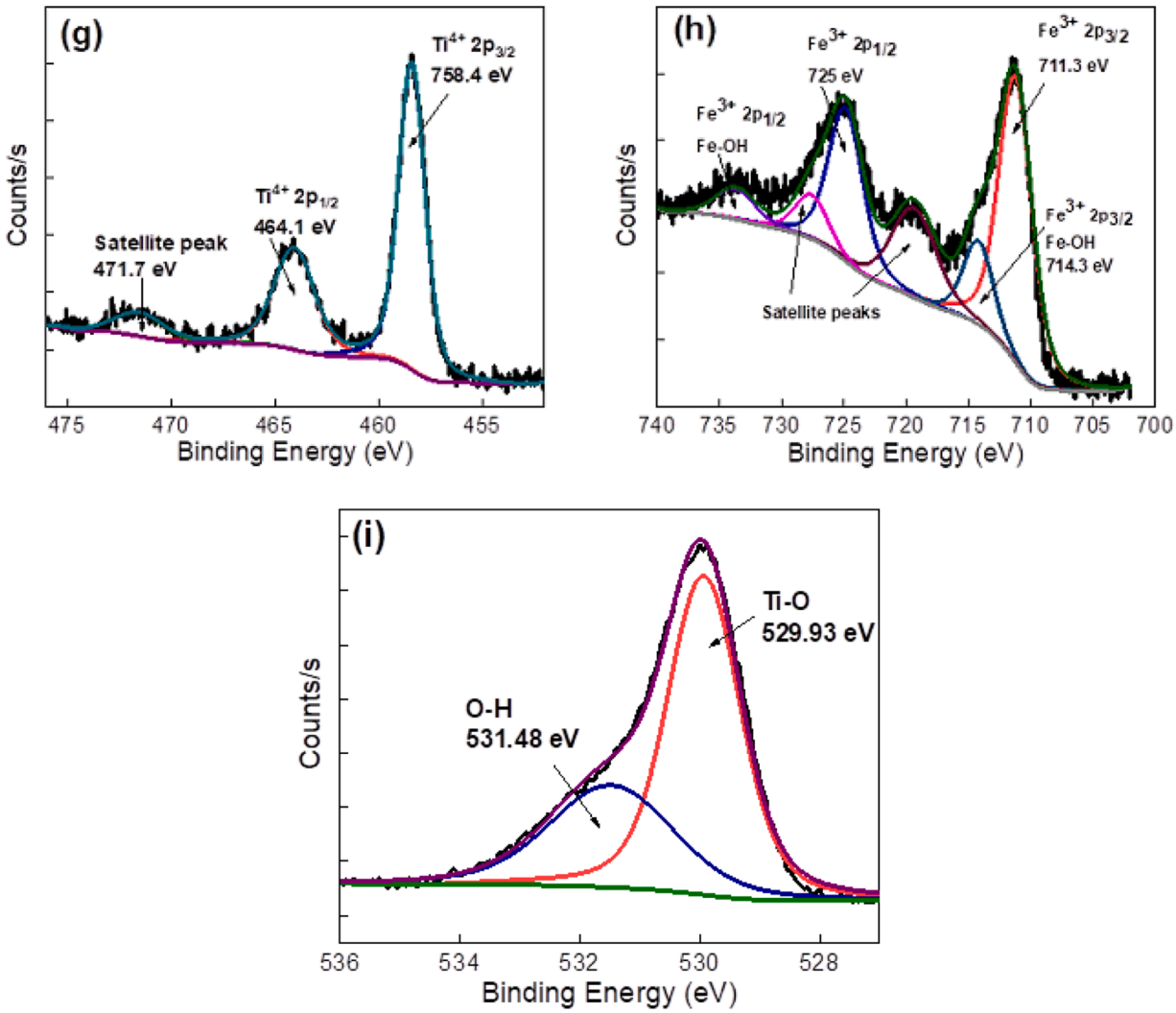

Fig. 4. (*continued*).

hybridized N in s-triazine rings (C-N=C), N-C_3, N atoms in the heptazine ring and as bridging atom, and π-excitations, respectively. The same chemical nature was observed in the higher resolution spectrum of N 1s of FFFGC40 (Fig. 4(f)) in which the respective peaks appeared at 398.6, 400, 400.7 and 404.9 eV, respectively. The higher resolution spectrum of Ti 2p of FFGC40 (Fig. 4(g)) shows the spin-orbital coupling where $2p_{3/2}$ and $2p_{1/2}$ peaks appeared at 458.4 eV and 464.1 eV confirming the presence of Ti^{4+}. The peak at 471.7 eV is attributed to the satellite peak. The higher resolution spectrum of Fe 2p (Fig. 4(h)) is deconvoluted to several peaks. Peaks at 711.3 and 725 eV correspond to the $2p_{3/2}$ and $2p_{1/2}$ peaks of Fe^{3+} indicating the spin-orbital coupling while the peaks at 719.5 and 733.9 eV represent the satellite peaks of them, respectively. The peak at 714.3 eV is assigned to the $2p_{3/2}$ of Fe^{3+} in the Fe-OH bond while the peak at 727.8 eV is attributed to the $2p_{1/2}$. The higher resolution spectrum of O 1s was deconvoluted to two peaks (Fig. 4(i)). The peak at 529.93 eV is attributed to Ti-O bond and the peak at 531.48 eV corresponds to the hydroxy or adsorbed water on the surface of the catalyst.

4.5. XRF analysis

The chemical composition of FF and FFGC40 was analyzed by XRF. The ratio of Fe to Ti is 2.6. Additionally, V and Mn were also detected because they are present in ilmenite sand in minor concentrations. The chemical composition of both FF and FFGC40 are almost the same and only C and N are present additionally in FGC40 (Table 1).

4.6. UV-Visible diffuse reflectance spectroscopic analysis

The optical properties of the synthesized nanocomposites were studied by UV-Visible diffuse reflectance spectroscopy. The optical absorbance was calculated using the Kubelka-Munk function ($\alpha = (1-R)^2/2R$). Here, α and R are the absorption coefficient and diffuse reflectance coefficient, respectively [50,51]. Tauc plots ($(F(R) \times h\nu)^n$ vs $h\nu$) indicating the direct transitions (n=2) of the synthesized composites are shown in Fig. 5. Extrapolations of direct transitions yield band gap values. The band gap value of GC is 2.63 eV being consistent with the literature [52] and that of FF nanoparticles is 2.76 eV. The band gap values of FFGC8, FFGC24 and FFGC40 are found to be 2.63, 2.80 and 2.63 eV, respectively, and they did not show a trend in variation. However, the band gap value decreased with an increasing proportion of FFT in FF8GC, FF24GC and FF40GC as 2.60, 2.48 and 2.50 eV, respectively. The band gap values are tabulated in Table 2. All the synthesized

Table 1
The chemical composition of the FF and FGC40 materials

Material	% Fe_2O_3	% TiO_2	% V_2O_5	% MnO_2
FF	70.25	27.83	0.68	1.24
FFGC40	72.23	25.79	0.64	1.33

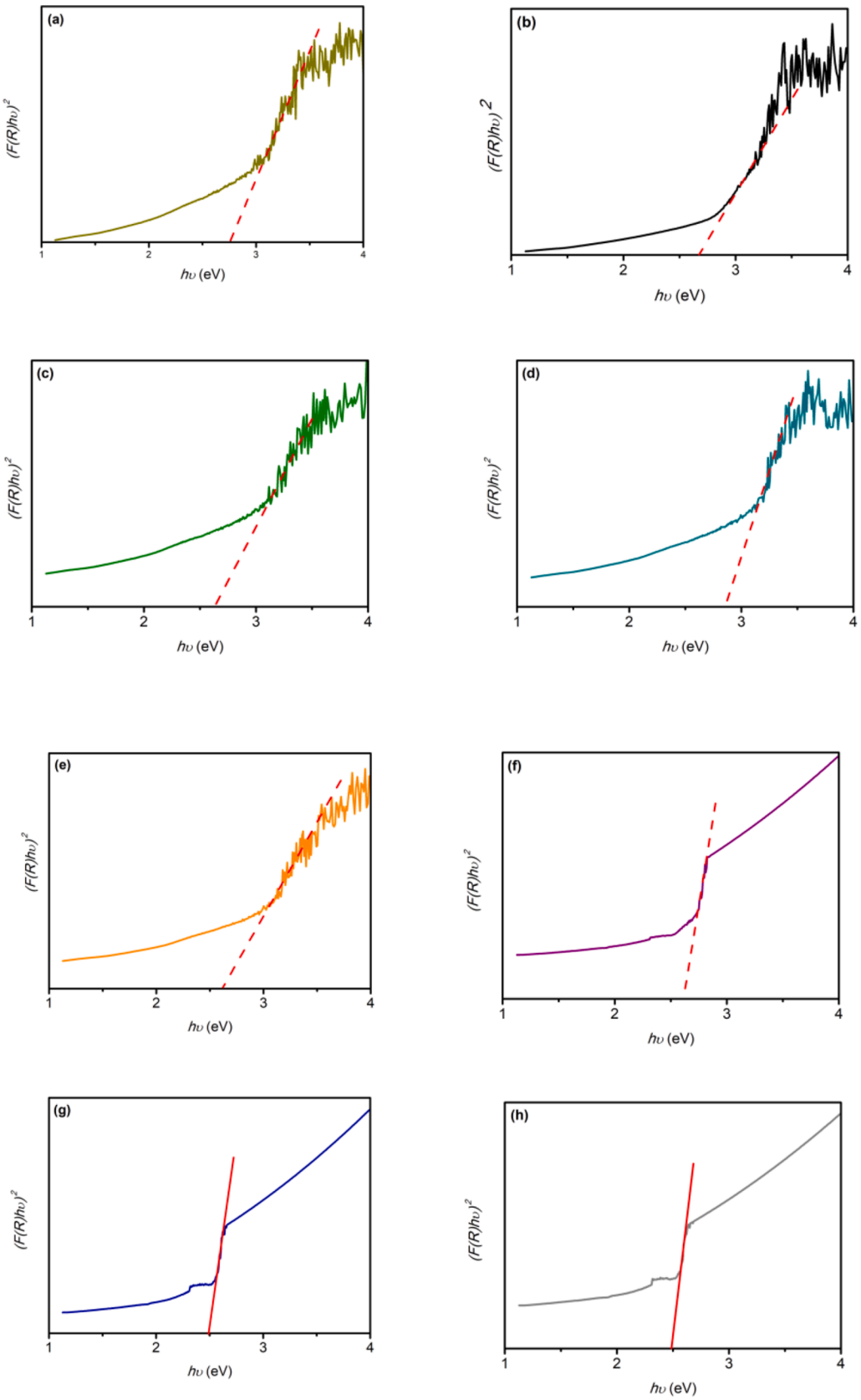

Fig. 5. Tauc plots indicating the direct transitions of (a) FF (b) GC (c) FF8GC (d) FF24GC (e) FF40GC (f) FFGC8 (g) FFGC24 (h) FFGC40.

Table 2
Rate constant for the photodegradation of methylene blue in the presence of synthesized photocatalysts.

Photocatalyst	Rate Constant (min^{-1})	Band Gap (eV)
GC	0.008	2.63
FF	0.007	2.76
FFGC8	0.001	2.63
FFGC24	0.005	2.86
FFGC40	0.009	2.63
FF8GC	0.006	2.60
FF24GC	0.006	2.48
FF40GC	0.004	2.50

composites efficiently absorb visible light as revealed by the calculated band gap values.

4.7. Photocatalytic activity

All the synthesized materials were shaken in MB solution for 90 minutes in dark to reach the adsorption-desorption equilibrium. Positively charged MB molecules form electrostatic interactions with the negatively charged FF nanoparticles and electron-rich g-C_3N_4. Variation of A/A_O with time is shown in Fig. 6 and the first-order kinetics for the photodegradation of MB are exhibited in Fig. 7. The highest initial rate constant (0.009 min^{-1}) for the degradation of methylene blue resulted in the presence of FFGC40. The initial rate constant for the photodegradation of MB in the presence of g-C_3N_4 and FF is 0.008 and 0.007 min^{-1}, respectively. FFGC40 contains the proper content of g-C_3N_4 (40%) with respect to the weight of FF, which facilitates the formation of the heterostructure at the interfaces of α-Fe_2O_3, Fe_2TiO_5 and g-C_3N_4 and thus enhances the absorption and utilization of sunlight. Further, the band gap of FFGC40 (2.63 eV) is lower than the other composites generally. Hence, the photodegradation of MB in the presence of FGC40 results is higher than in other composites. However, other composites were also active in producing the radicals required for the photodegradation, but the activity was lower due to the incomplete formation of the heterostructure. Further, the photocatalytic activity increased with an increasing percentage of g-C_3N_4 in the composites in which the content of g-C_3N_4 was varied, indicating that g-C_3N_4 facilitates the photocatalytic activity. Moreover, the initial rate constant of photodegradation of MB in the presence of FFGC8 (0.001 min^{-1}) and FFGC24 (0.005 min^{-1}) is lower than FF nanoparticles. This is due to the masking of FF nanoparticles by g-C_3N_4 and due to the improper ratio of FF and g-C_3N_4 to establish the correct alignment which could also lead to electron hole pair recombination. The rate of photodegradation of MB was dramatically decreased to 0.004 min^{-1} at the highest FF percentage (FF40GC) of the composites in which the FF content was varied because aggregated FF nanoparticles block the porous structure of g-C_3N_4 resulting in lower surface area limiting the adsorption of MB to the supporting matrix. Moreover, as the aggregated nanoparticles block the mesopore channels, the transport of the reactant molecules and products of degradation is slowed down. At lower percentages of FF, the photocatalytic activities were comparatively higher as sufficient g-C_3N_4 was available to be joined with FF phases to establish the heterostructure. The rate constants for the photodegradation of MB in the presence of the synthesized catalysts are tabulated in Table 2.

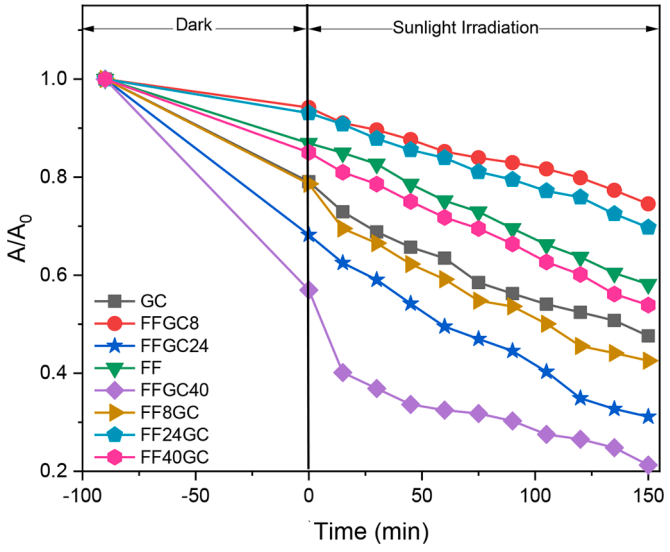

Fig. 6. Variation of A/A_O with time.

4.8. Mechanism of photodegradation

The structure-property engineering of semiconductor materials is important in degrading organic molecules [53]. The band gap values reported for α-Fe_2O_3, Fe_2TiO_5 and g-C_3N_4 are 2.0, 2.2 and 2.75 eV, respectively. The band edge potentials of the conduction band (E_{CB}) and the valence band (E_{VB}) can be calculated from the formula (1) and (2), respectively.

$$E_{CB} = X - -E^C - -0.5\,E_g$$

$$E_{VB} = X - -E^C + 0.5\,E_g$$

where X is the electronegativity of the semiconductor, which is the geometric mean of the electronegativity of the constituent atoms, and E^C is the energy of the free electrons on the hydrogen scale which is approximately 4.5. X values for α-Fe_2O_3, Fe_2TiO_5 and g-C_3N_4 are 4.78, 5.86 and 4.73, respectively. E_{CB} values of the above semiconductors are calculated to be -0.72, 0.26 and -1.15 V/normal hydrogen electrode (NHE), respectively, and the E_{VB} values of them are 1.28, 2.46 and 1.61 V/normal hydrogen electrode (NHE), respectively. The band alignment of the above semiconductors is shown in Scheme 1. Once the composites are exposed to sunlight electrons in the VB of all the semiconductors are excited to the CB leaving holes at the VB. According to Scheme 1(a). photogenerated electrons are migrated from the CB of α-Fe_2O_3 and g-C_3N_4 to the CB of Fe_2TiO_5 enriching the CB of Fe_2TiO_5 with electrons due to the favourable potential differences of the CBs. Photogenerated holes are migrated from the VB of Fe_2TiO_5 to the VB of α-Fe_2O_3 and the VB of g-C_3N_4. The CB potential of Fe_2TiO_5 (0.26 eV) is not enough to lead to the reduction of molecular O_2 to produce superoxide radicals ($O_2^{-\bullet}$) (-0.33 V). The VB positions of g-C_3N_4 (1.61 eV) and α-Fe_2O_3 (1.28 eV) are higher than the standard potentials of $OH^{\bullet}/OH^-$ (1.99 eV) and $OH^{\bullet}/H_2O$ (2.68 eV). Therefore, the h^+ cannot oxidize OH^- and H_2O to $OH^{\bullet}$. Therefore, radicals responsible for the photodegradation of MB would not be produced in type II ternary heterostructure band alignment. Scheme 1(b) shows the dual Z-scheme structure. An all-solid state Z-scheme heterostructure is consisted of two different semiconductors with an electron mediator to accomplish electron transfer from one semiconductor the other. However, a direct Z-scheme is comprised of two semiconductors which are linked with each other where an electron mediator is not essential. The photogenerated electrons and holes with high reduction and oxidizing ability are maintained by the recombination of electrons and holes in the second semiconductor [54]. According to that once the composite is exposed to sunlight photogenerated electrons excite to the CB of Fe_2TiO_5 are migrated to the VB of g-C_3N_4 and α-Fe_2O_3, which are then transferred to the VB of g-C_3N_4 and α-Fe_2O_3. Those transferred electrons produce $O_2^{-\bullet}$. Further, h^+ remaining in the VB of Fe_2TiO_5 with the potential of 2.46 eV generates $OH^{\bullet}$ by oxidation of OH^-. Hence, such produced both $O_2^{-\bullet}$ and $OH^{\bullet}$ would degrade MB. Further, in the presence of sunlight methylene blue molecules absorb light and excite electrons from HOMO level to LUMO level (gap 4.25 eV). The excited electron at the LUMO level could be lost and the holes at

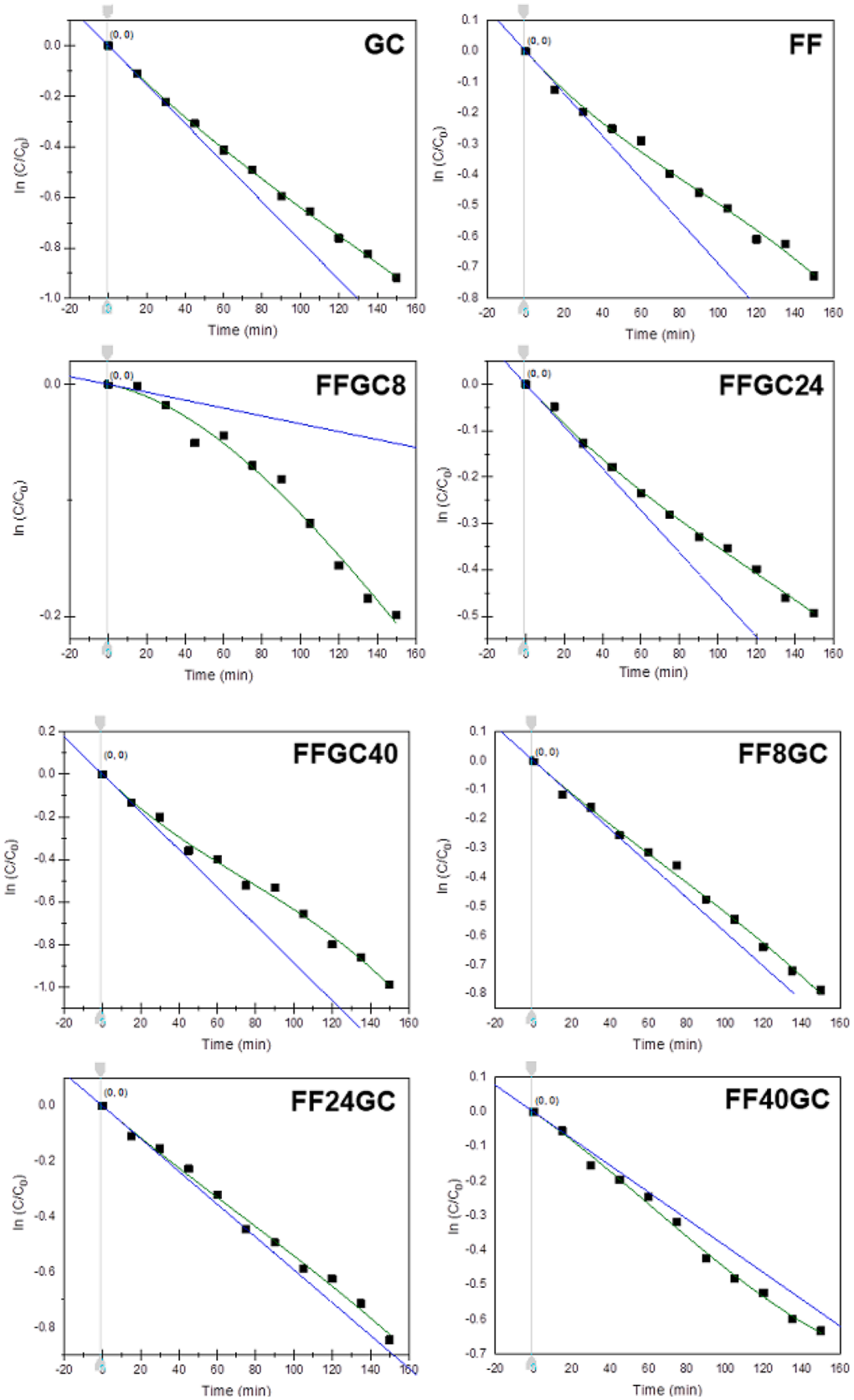

Fig. 7. First-order kinetics for photodegradation of MB under sunlight in the presence of synthesized photocatalysts.

the HOMO level require electrons to gain stability. Thus, those holes capture electrons from water and produce hydroxyl radicals which degrade methylene blue molecules further [55].

Photocatalytic activity of the best-performing catalyst FFGC40 was further performed in the presence of scavengers to confirm the mechanism proposed under visible light. Ethylenediaminetetraacetic acid (EDTA) and isopropyl alcohol (IPA) in the concentration of 4 mmol/dm^{-3} were used as the scavengers as they hunt holes and hydroxyl radicals, respectively (Fig. 8(a)). The rate of photocatalysis was dropped to 1.0×10^{-3} min^{-1} in the presence of both EDTA and IPA from 1.5×10^{-3} min^{-1} indicating that both holes and hydroxyl radicals mainly contribute to the photodegradation of MB. Interestingly, the initial rate of photodegrading MB in the presence of IPA is higher as could be seen with the drop of absorbance in the first 15 minutes which dramatically slowed down with time. This could be because initially with the addition of IPA the hydroxyl anion concentration increased which increased the hydroxyl radical concentration but with time IPA scavenge the hydroxyl radicals decreasing the photodegradation of MB. The effect of persulfate on the photocatalytic activity was determined by performing the reaction in the presence of 4 mmol/dm^{-3} $S_2O_8^{2-}$ (Fig. 8(b)) and the rate of reaction (38×10^{-2} min^{-1}) was found to be increased by 25 times because the $SO_4^{-\bullet}$ and $OH^{\bullet}$ produced by the reduction of $S_2O_8^{2-}$. Persulfate ions are reduced to $SO_4^{-\bullet}$ as shown in reaction 1 by the photogenerated electrons and such produced $SO_4^{-\bullet}$ reacts with OH^- in the medium to produce SO_4^{2-} and $OH^{\bullet}$ (reaction 2).

$$S_2O_8^{2-} + e^- \rightarrow SO_4^{-\bullet} + SO_4^{2-} \quad (1)$$

$$SO_4^{-\bullet} + OH^- \rightarrow SO_4^{2-} + OH^{\bullet} \quad (2)$$

The presence of different co-pollutants and change in the ionic strength on the photocatalytic activity was evaluated using 10 mmol/dm^{-3} Pb^{2+}, Rhodamine B, and $H_2PO_4^-$ as the co-pollutants and NaCl to change the ionic strength (Fig. 8(c)). The rate of the photodegradation of MB was dropped to 7.7×10^{-3} min^{-1}. Positively charged Pb^{2+} and MB both compete with the negatively charged catalyst surface. Small Pb^{2+} ions easily and readily adsorb to the catalyst surface restricting the adsorption of the bulky MB which leads to poor photocatalytic activity because the reactant molecules need to be close to the catalyst surface as the concentration of the reducing species is high. The rate constant for the photodegradation of MB was slightly decreased to 1.3×10^{-3} min^{-1} in the presence of Rhodamine B. Both MB and rhodamine B are positively charged bulky molecules where each type of the dye molecule competes with the other type on the surface of the catalyst. However, the rate was not drastically reduced as in the case with Pb^{2+} because both are bulky molecules and hence the competition to the catalyst surface would be the same. However, the reaction rate has not drastically reduced because though the catalyst surface is occupied by both MB and Rhodamine B molecules, the dye molecules adsorbed to the surface degrade upon exposure to light vacating the surface of the catalyst for the dye molecules in the solution. Further, the addition of NaCl has changed the ionic strength of the medium but hasn't changed the rate of the reaction (4.0×10^{-3} min^{-1}) significantly. However, the addition of $H_2PO_4^-$ has increased the rate of reaction to 3.3×10^{-3} min^{-1} because the phosphate ions accelerate the hydroxyl radical oxidation pathway [56].

The reusability of a catalyst is an important criterion that needs to be evaluated in catalysis, especially in commercialization. FFGC40 was selected for the study as it showed the highest photocatalytic activity. The efficiency of photodegrading MB by FFGC40 was reduced to 96.1% compared to the first cycle (Fig. 9). This could be because blockage of the porous system of g-C_3N_4 of the catalyst restricts the migration of the reactants to the heterojunctions limiting the reaction between MB molecules and radicals lowering the degradation of MB. Further, with prolonged use, metal oxide nanoparticles could leach out from the matrix reducing the concentration of the radicals formed. Moreover, there can be a loss of the catalyst after each cycle which also contributes to the reduction in the photocatalytic activity. Additionally, though the intensity of the sunlight available for all five cycles was in the range of 80000 - 1200000 lux during the experiments, variation of intensity affects the photocatalytic activity as well. However, it could be seen that FFGC40 could be used effectively for successive five cycles as shown in Fig. 9.

4.9. Antibacterial activity

The antibacterial activity of FF, FFGC40, FF40GC and GC was examined against gram-negative bacteria *E. Coli*. The maximum antibacterial activity (32.8%) was observed with FF40GC while that was followed by GC (28.7%) and FFGC40 (5.7%). FF showed no antibacterial activity. The antibacterial activity could be caused by four different mechanisms. (1) disrupt the cell wall by the nanocomposites (2) migration of nanocomposites into the cells and interfere with the ribosomes, and DNA replication and interrupt ATP production (3) disrupt

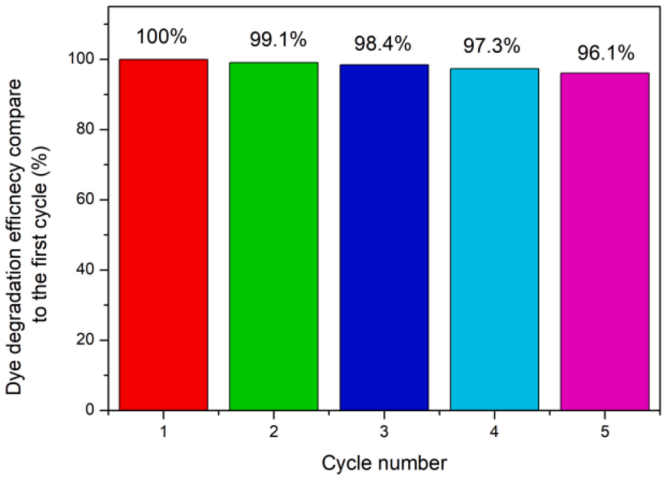

Fig. 9. Reusability of FFGC40 to photodegrade MB under sunlight.

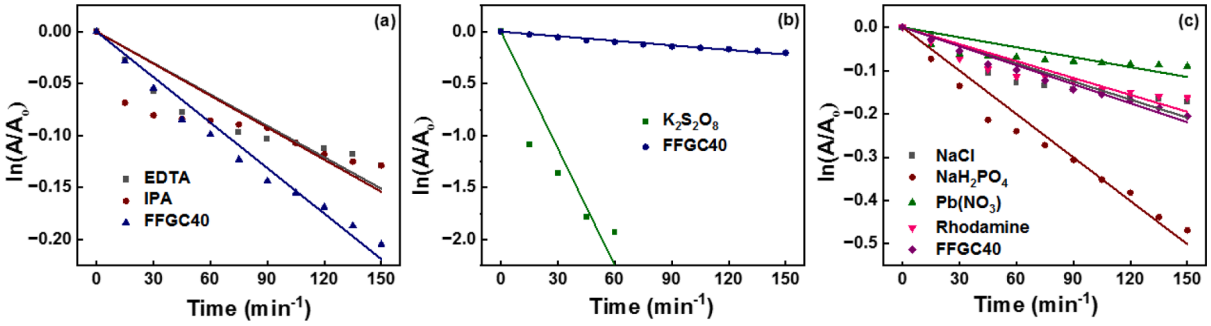

Fig. 8. Effect of (a) scavengers (b) $S_2O_8^{2-}$ and (c) ions and co-pollutants on photocatalysis

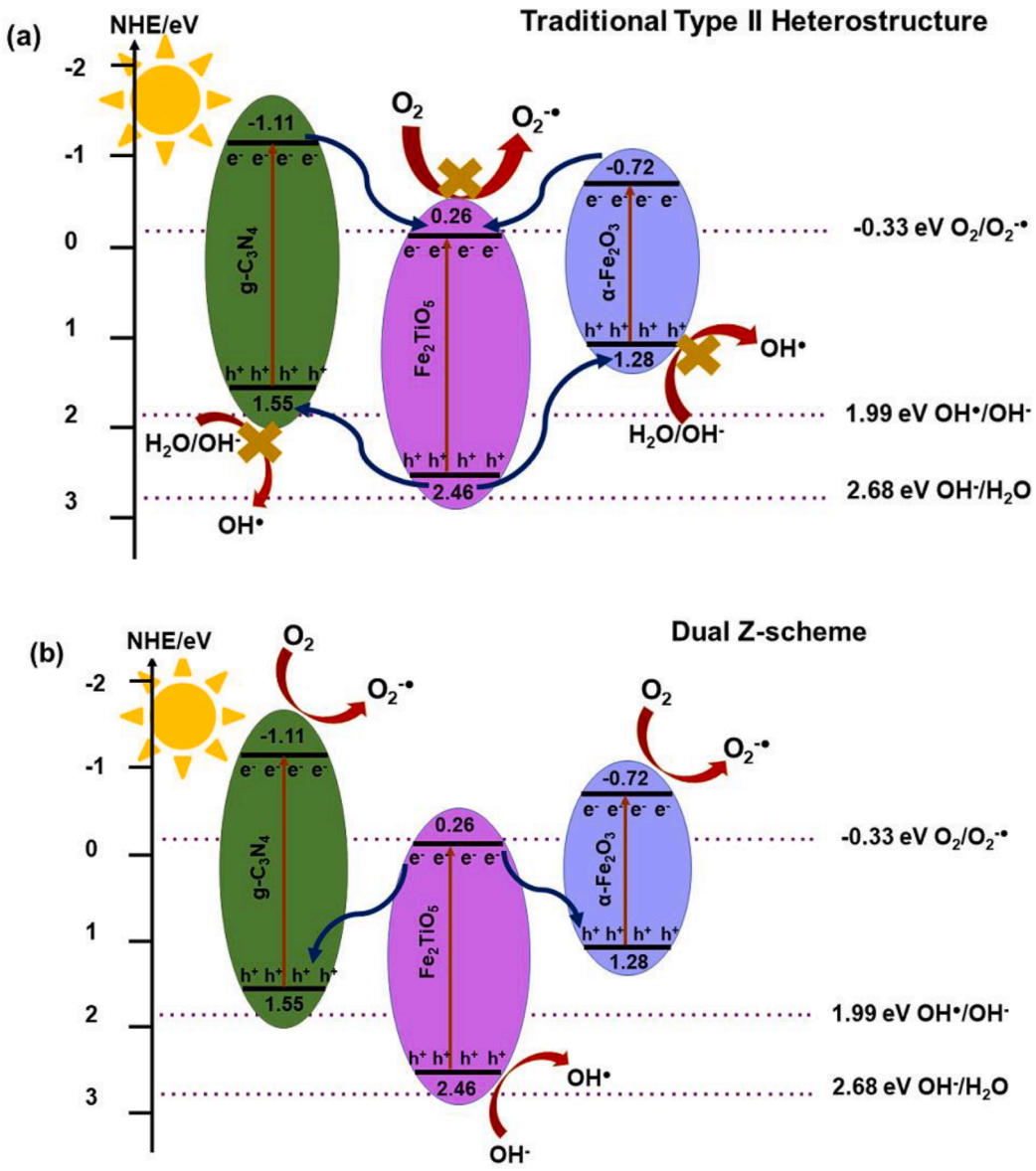

Scheme 1. Possible band alignment of the synthesized nanocomposite (a) Traditional type II heterostructure (b) Dual Z-scheme.

the membrane by reactive oxygen species (4) perforated membrane. GC which readily produces radicals in the visible range that showed the highest photocatalytic activity under the tested LED source would mainly inhibit bacteria via mechanism (3). However, FF40GC showed the highest antibacterial activity suggesting that mechanism (1), (2) and (4) also actively contribute as it could be assumed that the nanoparticles of FF40GC which has the highest nanoparticle concentration, enter the cell to facilitate the mechanism (2) contributing to (1) and (4). But as the FF which are only nanoparticles showed no antibacterial activity, it is considered that mechanism (3) greatly contributes together with mechanisms (1), (2) and (4). Antibacterial activity of GC is lower than that of FF40GC suggesting that though GC produces radicals which generate oxygen reactive species, the contribution via mechanisms (1), (2) and (4) is minimum due to the size factor and hence the resulting net antibacterial activity is lower than FF40GC, which inhibit the bacterial growth by all the four mechanisms. Meanwhile, FFGC40 exhibited a very low inhibition action though its nanoparticle concentration is higher than FF40GC because the FF nanoparticles mask the GC limiting the antibacterial activity of GC. As described above FF nanoparticles showed no antibacterial activity. Therefore, it is evident that the synthesized nanocomposites inhibit the growth of *E.Coli* at a concentration of 60 mg/ml.

5. Conclusions

g-C_3N_4/Fe_2TiO_5/α-Fe_2O_3 ternary nanocomposites with closely contacted interfaces were successfully fabricated by using urea and natural ilmenite sand as the raw materials via the hydrothermal method adding value to the ilmenite mineral. g-C_3N_4/Fe_2TiO_5/α-Fe_2O_3 ternary nanocomposites showed higher photocatalytic activity than g-C_3N_4 and Fe_2TiO_5/α-Fe_2O_3 for the photodegradation of methylene blue under sunlight. Newly fabricated catalyst is high in activity than other iron oxide and g-C_3N_4 catalysts reported in the literature. The enhanced photocatalytic activity is ascribed to the efficient transfer of photogenerated electrons and holes between g-C_3N_4, Fe_2TiO_5 and α-Fe_2O_3. The present study demonstrates that engineering new heterostructures is promising in fabricating new photocatalysts for the degradation of organic pollutants in wastewater.

Funding statement

This research was supported by the Accelerating Higher Education

Expansion and Development (AHEAD) Operation of the Ministry of Higher Education funded by the World Bank.

Declaration of Competing Interest

The authors declare that they have no known competing financial interests or personal relationships that could have appeared to influence the work reported in this paper.

Data availability

The data that has been used is confidential.

Acknowledgment

The authors acknowledge the Sri Lanka Institute of Nanotechnology, University of Peradeniya, University of Moratuwa and Indian institute of technology, Delhi for providing the instrument facilities.

References

[1] M.T. Yagub, T.K. Sen, S. Afroze, H.M. Ang, Dye and its removal from aqueous solution by adsorption: A review, Adv. Colloid Interface Sci. 209 (2014) 172–184, https://doi.org/10.1016/J.CIS.2014.04.002. Jul.

[2] V. Katheresan, J. Kansedo, S.Y. Lau, Efficiency of various recent wastewater dye removal methods: A review, J. Environ. Chem. Eng. 6 (4) (2018) 4676–4697, https://doi.org/10.1016/J.JECE.2018.06.060. Aug.

[3] P.B. Ramos, P. Vitale, G.P. Barreto, F. Aparicio, M.D.L.Á. Dublan, G.N. Eyler, Treatment of real non-biodegradable wastewater: Feasibility analysis of a zero-valent iron/H2O2process, J. Environ. Chem. Eng. 8 (4) (2020), 103954, https://doi.org/10.1016/j.jece.2020.103954. Aug.

[4] M. Suzuki, Y. Suzuki, K. Uzuka, Y. Kawase, Biological treatment of non-biodegradable azo-dye enhanced by zero-valent iron (ZVI) pre-treatment, Chemosphere 259 (2020), 127470, https://doi.org/10.1016/j.chemosphere.2020.127470. Nov.

[5] A.B. dos Santos, F.J. Cervantes, J.B. van Lier, Review paper on current technologies for decolourisation of textile wastewaters: Perspectives for anaerobic biotechnology, Bioresource Technology 98 (12) (2007) 2369–2385, https://doi.org/10.1016/j.biortech.2006.11.013. Sep. 01.

[6] C.R. Holkar, A.J. Jadhav, D.V. Pinjari, N.M. Mahamuni, A.B. Pandit, A critical review on textile wastewater treatments: Possible approaches, Journal of Environmental Management 182 (2016) 351–366, https://doi.org/10.1016/j.jenvman.2016.07.090. Nov. 01.

[7] K.Z. Elwakeel, A.M. Elgarahy, G.A. Elshoubaky, S.H. Mohammad, Microwave assist sorption of crystal violet and Congo red dyes onto amphoteric sorbent based on upcycled Sepia shells 03 Chemical Sciences 0306 Physical Chemistry (incl. Structural), J. Environ. Heal. Sci. Eng. 18 (1) (2020) 35–50, https://doi.org/10.1007/s40201-019-00435-1. Jan.

[8] K.P. Sharma, et al., A comparative study on characterization of textile wastewaters (untreated and treated) toxicity by chemical and biological tests, Chemosphere 69 (1) (2007) 48–54, https://doi.org/10.1016/J.CHEMOSPHERE.2007.04.086. Aug.

[9] F.M.D. Chequer, G.A.R. de Oliveira, E.R.A. Ferraz, J.C. Cardoso, M.V.B. Zanoni, D. P. de Oliveira, Textile Dyes: Dyeing Process and Environmental Impact, Eco-Friendly Text. Dye. Finish. (2013), https://doi.org/10.5772/53659. Jan.

[10] S. Madan, R. Shaw, S. Tiwari, S.K. Tiwari, Adsorption dynamics of Congo red dye removal using ZnO functionalized high silica zeolitic particles, Appl. Surf. Sci. 487 (2019) 907–917, https://doi.org/10.1016/j.apsusc.2019.04.273. Sep.

[11] A.H. Jawad, R. Razuan, J.N. Appaturi, L.D. Wilson, Adsorption and mechanism study for methylene blue dye removal with carbonized watermelon (Citrullus lanatus)rind prepared via one-step liquid phase H 2 SO 4 activation, Surfaces and Interfaces 16 (2019) 76–84, https://doi.org/10.1016/j.surfin.2019.04.012. Sep.

[12] L. Mais, A. Vacca, M. Mascia, E.M. Usai, S. Tronci, S. Palmas, Experimental study on the optimisation of azo-dyes removal by photo-electrochemical oxidation with TiO2 nanotubes, Chemosphere 248 (2020), 125938, https://doi.org/10.1016/j.chemosphere.2020.125938. Jun.

[13] J. Li, K. Zhu, R. Li, X. Fan, H. Lin, H. Zhang, The removal of azo dye from aqueous solution by oxidation with peroxydisulfate in the presence of granular activated carbon: Performance, mechanism and reusability, Chemosphere 259 (2020), 127400, https://doi.org/10.1016/j.chemosphere.2020.127400. Nov.

[14] H. Demissie, G. An, R. Jiao, T. Ritigala, S. Lu, D. Wang, Modification of high content nanocluster-based coagulation for rapid removal of dye from water and the mechanism, Sep. Purif. Technol. 259 (2021), 117845, https://doi.org/10.1016/j.seppur.2020.117845. Mar.

[15] M.J. Puchana-Rosero, E.C. Lima, B. Mella, D. Da Costa, E. Poll, M. Gutterres, A coagulation-flocculation process combined with adsorption using activated carbon obtained from sludge for dye removal from tannery wastewater, J. Chil. Chem. Soc. 63 (1) (2018) 3867–3874, https://doi.org/10.4067/s0717-97072018000103867.

[16] X. Wang, et al., New surface cross-linking method to fabricate positively charged nanofiltration membranes for dye removal, J. Chem. Technol. Biotechnol. 93 (8) (2018) 2281–2291, https://doi.org/10.1002/jctb.5571. Aug.

[17] X. Yang, F. You, Y. Zhao, Y. Bai, L. Shao, Confinedly Assembling Surface Nanocoating to Manipulate Nanofiltration Membranes for Highly-efficient Dye Removal, ES Energy Environ (2018), https://doi.org/10.30919/esee8c142.

[18] B. Van der Bruggen, M. Mänttäri, M. Nyström, Drawbacks of applying nanofiltration and how to avoid them: A review, Separation and Purification Technology 63 (2) (2008) 251–263, https://doi.org/10.1016/j.seppur.2008.05.010. Oct. 22,.

[19] G. Crini, E. Lichtfouse, Advantages and disadvantages of techniques used for wastewater treatment, Environmental Chemistry Letters 17 (1) (2019) 145–155, https://doi.org/10.1007/s10311-018-0785-9. Mar. 01,.

[20] S. Cheng, et al., Emerging Strategies for CO2 Photoreduction to CH4: From Experimental to Data-Driven Design, Adv. Energy Mater. 12 (20) (2022), 2200389, https://doi.org/10.1002/AENM.202200389. May.

[21] N. Modirshahla, M.A. Behnajady, R. Rahbarfam, A. Hassani, Effects of Operational Parameters on Decolorization of C. I. Acid Red 88 by UV/H2O2 Process: Evaluation of Electrical Energy Consumption, CLEAN – Soil, Air, Water 40 (3) (2012) 298–302, https://doi.org/10.1002/CLEN.201000574. Mar.

[22] A.V. Karim, A. Hassani, P. Eghbali, P.V. Nidheesh, Nanostructured modified layered double hydroxides (LDHs)-based catalysts: A review on synthesis, characterization, and applications in water remediation by advanced oxidation processes, Curr. Opin. Solid State Mater. Sci. 26 (1) (2022), 100965, https://doi.org/10.1016/J.COSSMS.2021.100965. Feb.

[23] H. Wang, et al., A review on heterogeneous photocatalysis for environmental remediation: From semiconductors to modification strategies, Chinese J. Catal. 43 (2) (2022) 178–214, https://doi.org/10.1016/S1872-2067(21)63910-4. Feb.

[24] X. Wang, et al., A metal-free polymeric photocatalyst for hydrogen production from water under visible light, Nat. Mater. 8 (1) (2009) 76–80, https://doi.org/10.1038/nmat2317. *81*Nov. 2008.

[25] Q. Li, L. Zong, Y. Xing, X. Wang, L. Yu, J. Yang, Preparation of g-C3N4/TiO2 nanocomposites and investigation of their photocatalytic activity, Sci. Adv. Mater. 5 (9) (2013) 1316–1322, https://doi.org/10.1166/SAM.2013.1589.

[26] H. Liu, et al., Fabrication of surface alkalinized g-C3N4 and TiO2 composite for the synergistic adsorption-photocatalytic degradation of methylene blue, Appl. Surf. Sci. 473 (2019) 855–863, https://doi.org/10.1016/J.APSUSC.2018.12.162. Apr.

[27] N. Zhang, J. Gao, C. Huang, W. Liu, P. Tong, L. Zhang, In situ hydrothermal growth of ZnO/g-C3N4 nanoflowers coated solid-phase microextraction fibers coupled with GC-MS for determination of pesticides residues, Anal. Chim. Acta 934 (2016) 122–131, https://doi.org/10.1016/J.ACA.2016.06.029. Aug.

[28] E. Jang, D.W. Kim, S.H. Hong, Y.M. Park, T.J. Park, Visible light-driven g-C3N4@ZnO heterojunction photocatalyst synthesized via atomic layer deposition with a specially designed rotary reactor, Appl. Surf. Sci. 487 (2019) 206–210, https://doi.org/10.1016/J.APSUSC.2019.05.035. Sep.

[29] S. Ye, L.G. Qiu, Y.P. Yuan, Y.J. Zhu, J. Xia, J.F. Zhu, Facile fabrication of magnetically separable graphitic carbon nitride photocatalysts with enhanced photocatalytic activity under visible light, J. Mater. Chem. A 1 (9) (2013) 3008–3015, https://doi.org/10.1039/C2TA01069K. Feb.

[30] M. Wang, S. Cui, X. Yang, W. Bi, Synthesis of g-C3N4/Fe3O4 nanocomposites and application as a new sorbent for solid phase extraction of polycyclic aromatic hydrocarbons in water samples, Talanta 132 (2015) 922–928, https://doi.org/10.1016/J.TALANTA.2014.08.071. Jan.

[31] A. Seza, et al., Novel microwave-assisted synthesis of porous g-C3N4/SnO2 nanocomposite for solar water-splitting, Appl. Surf. Sci. 440 (2018) 153–161, https://doi.org/10.1016/J.APSUSC.2018.01.133. May.

[32] Y. Zang, L. Li, X. Li, R. Lin, G. Li, Synergistic collaboration of g-C3N4/SnO2 composites for enhanced visible-light photocatalytic activity, Chem. Eng. J. 246 (2014) 277–286, https://doi.org/10.1016/J.CEJ.2014.02.068. Jun.

[33] C. Cheng, J. Shi, Y. Hu, L. Guo, WO3/g-C3N4 composites: one-pot preparation and enhanced photocatalytic H2 production under visible-light irradiation, Nanotechnology 28 (16) (2017), 164002, https://doi.org/10.1088/1361-6528/AA651A. Mar.

[34] X. Zhang, S. He, S.P. Jiang, WOx/g-C3N4 layered heterostructures with controlled crystallinity towards superior photocatalytic degradation and H2 generation, Carbon N. Y. 156 (2020) 488–498, https://doi.org/10.1016/J.CARBON.2019.09.083. Jan.

[35] T. Jayaraman, S. Arumugam Raja, A. Priya, M. Jagannathan, M. Ashokkumar, Synthesis of a visible-light active V2O5–g-C3N4 heterojunction as an efficient photocatalytic and photoelectrochemical material, New J. Chem. 39 (2) (2015) 1367–1374, https://doi.org/10.1039/C4NJ01807A. Feb.

[36] Q. Liu, C. Fan, H. Tang, X. Sun, J. Yang, X. Cheng, One-pot synthesis of g-C3N4/V2O5 composites for visible light-driven photocatalytic activity, Appl. Surf. Sci. 358 (2015) 188–195, https://doi.org/10.1016/J.APSUSC.2015.09.010. Dec.

[37] A. Hassani, P. Eghbali, Ö. Metin, Sonocatalytic removal of methylene blue from water solution by cobalt ferrite/mesoporous graphitic carbon nitride (CoFe2O4/mpg-C3N4) nanocomposites: response surface methodology approach, Environ. Sci. Pollut. Res. 25 (32) (2018) 32140–32155, https://doi.org/10.1007/S11356-018-3151-3. *2018 2532*Sep.

[38] A. Hassani, M. Faraji, P. Eghbali, Facile fabrication of mpg-C3N4/Ag/ZnO nanowires/Zn photocatalyst plates for photodegradation of dye pollutant, J. Photochem. Photobiol. A Chem. 400 (2020), 112665, https://doi.org/10.1016/J.JPHOTOCHEM.2020.112665. Sep.

[39] A. Kumar, et al., Construction of dual Z-scheme g-C3N4/Bi4Ti3O12/Bi4O5I2 heterojunction for visible and solar powered coupled photocatalytic antibiotic degradation and hydrogen production: Boosting via I−/I3− and Bi3+/Bi5+ redox

mediators, Appl. Catal. B Environ. 284 (2021), 119808, https://doi.org/10.1016/J.APCATB.2020.119808. May.
[40] W. Liu, J. Shen, X. Yang, Q. Liu, H. Tang, Dual Z-scheme g-C3N4/Ag3PO4/Ag2MoO4 ternary composite photocatalyst for solar oxygen evolution from water splitting, Appl. Surf. Sci. 456 (2018) 369–378, https://doi.org/10.1016/J.APSUSC.2018.06.156. Oct.
[41] L. Jiang, et al., In-situ synthesis of direct solid-state dual Z-scheme WO3/g-C3N4/Bi2O3 photocatalyst for the degradation of refractory pollutant, Appl. Catal. B Environ. 227 (2018) 376–385, https://doi.org/10.1016/J.APCATB.2018.01.042. Jul.
[42] H.Y. Liu, et al., Facile assembly of g-C3N4/Ag2CO3/graphene oxide with a novel dual Z-scheme system for enhanced photocatalytic pollutant degradation, Appl. Surf. Sci. 475 (2019) 421–434, https://doi.org/10.1016/J.APSUSC.2019.01.018. May.
[43] T. Charitha, U. Leshan, M. Shanitha, W. Ramanee, L. Buddi, B. Martin, Efficient photodegradation activity of α-Fe2O3/Fe2TiO5/TiO2 and Fe2TiO5/TiO2 nanocomposites synthesized from natural ilmenite, Results Mater. 12 (2021), 100219, https://doi.org/10.1016/J.RINMA.2021.100219. Dec.
[44] C. Thambiliyagodage, S. Mirihana, R. Wijesekera, D.S. Madusanka, M. Kandanapitiye, M. Bakker, Fabrication of Fe2TiO5/TiO2 binary nanocomposite from natural ilmenite and their photocatalytic activity under solar energy, Curr. Res. Green Sustain. Chem. 4 (2021), 100156, https://doi.org/10.1016/J.CRGSC.2021.100156. Jan.
[45] P. Nuengmatcha, P. Porrawatkul, S. Chanthai, P. Sricharoen, N. Limchoowong, Enhanced photocatalytic degradation of methylene blue using Fe2O3/graphene/CuO nanocomposites under visible light, J. Environ. Chem. Eng. 7 (6) (2019), 103438, https://doi.org/10.1016/J.JECE.2019.103438. Dec.
[46] S. Madihi-Bidgoli, S. Asadnezhad, A. Yaghoot-Nezhad, A. Hassani, Azurobine degradation using Fe2O3@multi-walled carbon nanotube activated peroxymonosulfate (PMS) under UVA-LED irradiation: performance, mechanism and environmental application, J. Environ. Chem. Eng. 9 (6) (2021), 106660, https://doi.org/10.1016/J.JECE.2021.106660. Dec.
[47] D.E. Fouad, C. Zhang, H. El-Didamony, L. Yingnan, T.D. Mekuria, A.H. Shah, Improved size, morphology and crystallinity of hematite (α-Fe2O3) nanoparticles synthesized via the precipitation route using ferric sulfate precursor, Results Phys 12 (2019) 1253–1261, https://doi.org/10.1016/j.rinp.2019.01.005. Mar.
[48] Z. Zhao, Y. Sun, Q. Luo, F. Dong, H. Li, and W. K. Ho, "Mass-Controlled Direct Synthesis of Graphene-like Carbon Nitride Nanosheets with Exceptional High Visible Light Activity. Less is Better," *Sci. Reports* 2015 *51*, vol. 5, no. 1, pp. 1–15, Sep. 2015, doi: 10.1038/srep14643.
[49] J. Liu, T. Zhang, Z. Wang, G. Dawson, W. Chen, Simple pyrolysis of urea into graphitic carbon nitride with recyclable adsorption and photocatalytic activity, J. Mater. Chem. 21 (38) (2011) 14398–14401, https://doi.org/10.1039/C1JM12620B. Sep.
[50] Q. Li, R. Xie, W.L. Yin, E.A. Mintz, K.S. Jian, Enhanced visible-light-induced photocatalytic disinfection of E. coli by carbon-sensitized nitrogen-doped titanium oxide, Environ. Sci. Technol. 41 (14) (2007) 5050–5056, https://doi.org/10.1021/es062753c. Jul.
[51] K. Xiong, et al., Heterostructured ZnFe2O4/Fe2TiO5/TiO2 Composite Nanotube Arrays with an Improved Photocatalysis Degradation Efficiency Under Simulated Sunlight Irradiation, Nano-Micro Lett 10 (1) (2018), https://doi.org/10.1007/s40820-017-0169-x. Jan.
[52] D. Long, H. Dou, X. Rao, Z. Chen, Y. Zhang, Z-Scheme Ag3PO4/g-C3N4 Nanocomposites for Robust Cocatalyst-Free Photocatalytic H2 Evolution Under Visible Light Irradiation, Catal. Lett. 149 (5) (2019) 1154–1166, https://doi.org/10.1007/S10562-019-02704-Y. *2019 1495*Feb.
[53] N. Uddin, H. Zhang, Y. Du, G. Jia, S. Wang, Z. Yin, Structural-Phase Catalytic Redox Reactions in Energy and Environmental Applications, Adv. Mater. 32 (9) (2020), 1905739, https://doi.org/10.1002/ADMA.201905739. Mar.
[54] A. Hassani, S. Krishnan, J. Scaria, P. Eghbali, P.V. Nidheesh, Z-scheme photocatalysts for visible-light-driven pollutants degradation: A review on recent advancements, Curr. Opin. Solid State Mater. Sci. 25 (5) (2021), 100941, https://doi.org/10.1016/J.COSSMS.2021.100941. Oct.
[55] N. Pourshirband, A. Nezamzadeh-Ejhieh, An efficient Z-scheme CdS/g-C3N4 nano catalyst in methyl orange photodegradation: Focus on the scavenging agent and mechanism, J. Mol. Liq. 335 (2021), 116543, https://doi.org/10.1016/J.MOLLIQ.2021.116543. Aug.
[56] D. Zhao, et al., Surface Modification of TiO2 by Phosphate: Effect on Photocatalytic Activity and Mechanism Implication, J. Phys. Chem. C 112 (15) (2008) 5993–6001, https://doi.org/10.1021/jp712049c. Apr.